Segregation of copper oxide on calcium copper titanate surface induced by Graphene Oxide for Water splitting applications

Sara Kawrani, Madona Boulos, Maged Bekheet, Roman Viter, Amr Nada, Wiebke Riedel, Stéphanie Roualdes, David Cornu, Mikhael Bechelany

Segregation of copper oxide on calcium copper titanate surface induced by Graphene Oxide for Water splitting applications

Sara Kawrani [a,b], Madona Boulos [b], Maged F.Bekheet [c], Roman Viter[d,e], Amr A. Nada[a,f], Wiebke Riedel[j], Stéphanie Roualdes[a], David Cornu [a], Mikhael Bechelany [a]*

[a] Institut Européen des Membranes, IEM, UMR-5635, Univ Montpellier, ENSCM, CNRS, Montpellier, France

[b] Laboratoire de Chimie Physique des matériaux, Université Libanaise, Liban

[c] Fachgebiet Keramische Werkstoffe/Chair of Advanced Ceramic materials, Institut für Werkstoffwissenschaften und -technologien, Technische Universität Berlin, Hardenbergstraße 40, 10623 Berlin, Germany

[d] Institute of Atomic Physics and Spectroscopy, University of Latvia, 19 Raina Blvd., LV 1586, Riga, Latvia

[e] Sumy State University, Center for Collective Use of Scientific Equipment 31, Sanatornaya st., 40018, Sumy, Ukraine

[f] Dept. of Analysis and Evaluation, Egyptian Petroleum Research Institute, Cairo, Nasr City, P.B. 11727, Egypt

[j] Institut für Chemie, Freie Universität Berlin, Arnimallee 22, 14195 Berlin, Germany

**Corresponding author: mikhael.bechelany@umontpellier.fr*

Abstract

Photoelectrochemical cells (PEC) are promised devices for hydrogen production via sunlight energy. One of the important challenges in this area is to design photoactive electrodes able to absorb visible light. A good photoelectrochemical behavior depends on the presence of surface active sites to photogenerate current at the lower possible potential for water splitting. Recent investigations in this field are focusing on perovskite materials such as $CaCu_3Ti_4O_{12}$ (CCTO) as visible light active electrode due its outstanding structure in which CCTO enclose in its structure a visible light absorbance component (CuO). The presence CuO on the material surface is mainly responsible for trapping electrons. Therefore, CCTO photoelectrocatalysts were prepared using different amounts of graphene oxide (GO) in this work. Physico-chemical characterizations showed that the oxydation of GO at high

temperatures lead to the reduction of Ti^{4+} to Ti^{3+} and Cu^{2+} to Cu^{+}, causing a segregation of copper on grain boundaries regions as revealed by X-ray diffraction (XRD), scanning electron microscopy (SEM), X-ray photoelectron spectroscopy (XPS) and Raman characterizations. Electrochemical performance and materials resistivity are measured in dark and under visible light irradiation. CCTO prepared using 3% of GO showed 50% higher photocurrent generation and hydrogen generation rate than pure phase of CCTO.

Key words

- Water splitting
- Photoelectrochemical cell
- Perovskite $CaCu_3Ti_4O_{12}$
- Graphene oxide
- Ti^{4+} reduction
- Cu^{2+} reduction

Graphical abstract

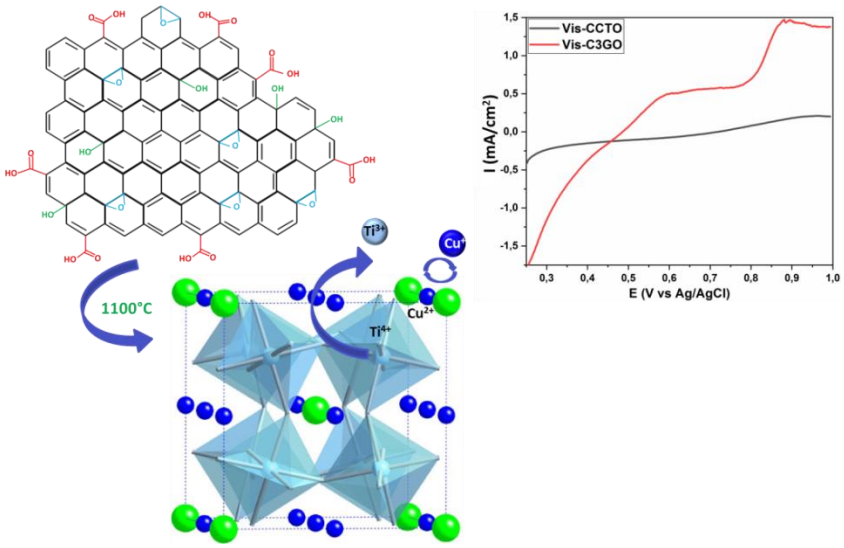

1. Introduction

Currently, a high amount of the global primarily energy need is met by burning fossil fuels. This directly impact the environment and put modern society in front of insufficient energy

sources [1], [2]. To address these issues, new renewable energy systems are needed. Hydrogen is an efficient energy carrier that can combine with oxygen in a fuel cell to produce electricity without generating pollutants [3]. However, the main methods to produce hydrogen comes from steam reforming of natural gas, in which the production demands a consumption of natural resources and induces the formation of carbon dioxide as byproduct [4]. Photoelectrochemical water splitting systems are studied widely, due to their efficient hydrogen production, without pollutant generation [5]. The produced hydrogen from Photo electrochemical cells (PEC) is still not well investigated in comparison to the traditional method; especially that it is limited by the used photoelectrodes. To achieve solar-water-splitting, PEC system employs photoactive semiconductors able to absorb solar light to produce electrons and holes and generate the photovoltage needed to split water [6]. Since the photoelectrochemical performance depends largely from the stability and efficiency of photoelectrodes, large number of catalysts has been investigated including composites. Noble-metals-based such as Platinum, oxides based Ruthenium (RuO_2) and Iridium (IrO_2) were used as electrodes and show excellent efficiency [7]–[9]. The activity of such photoelectrodes is limited by their instability in alkaline solution, high cost and poor abundant. Carbon-based materials (graphene, graphene oxide, g-C_3N_4) achieve considerable attention due their chemical and optical properties [10], [11]. Nevertheless, their intrinsic inconvenient of bulks such as low surface and high recombination efficiency of photogenerated electron-holes pairs limit the carbon based materials performance under visible light [12]. Spinel materials known as metal oxide ($A'B'_2O_4$; A'=alkaline-earth and/or transition metals, B'=group 13 elements and /or transition metals) had been investigated as well due to their enhanced electrocatalytic activity under visible light [13], [14]. However, the lack of fundamental studies on the limiting factors affected their behavior has prohibited important advance in their performance.

Perovskite materials (ABO_3 where A= Alkaline earth and or/transition metals and B= transition metals) were widely studied due to its bifunctional electrocatalytic behavior [15]–[17]. Among them, $CaCu_3Ti_4O_{12}$ (CCTO) known as high dielectric material is a double perovskite with a cubic structure ($A'ABO_3$), where A' and A site are occupied by Ca^{2+} and Cu^{2+} and Ti^{4+} is localized at B site [18]. CCTO structure is characterized by incorporating of Ti^{4+} and the open-shell Cu^{2+} into the perovskite without any doping. A distortion of TiO_6 octahedra in the structure forms a square planar structure to produce Jahn-Teller distortion in Cu^{2+}[19]. However the strong covalence bonding of oxygen atom with A'-Cu and B-Ti ions enhance the charge transfer between them, which is a key in electrocatalytic activity [20].

Since those photocatalytic and photoelectrochemical performances of a catalyst mainly depend on light absorption, CCTO is chosen like a candidate because it is a combination from TiO_2 catalyst highly active under UV light irradiation and CuO able to absorb visible light [21], [22]. The prepared nanocomposites are n-type materials, so it is more suitable for the OER than for the HER. The oxygen evolution reaction is the complementary anodic half reaction in electrochemical water splitting. The OER is the more complex of the two half reactions and is consequently responsible for the majority of inefficiency in the electrophotocatalytic devices.

However the electrocatalytic performance of these materials is still poor due to their large band gap, low active sites and weak electrical conductivity. Recently many defect engineering studies are focusing on the creation of oxygen vacancies in order to obtain superior electrocatalytic performance for these materials. It is known that oxygen vacancies are catalytically active sites and their presence in materials is able to regulate its electronic structure and serve as reactive species [23]. Hailili *et al.* [24] prepared by molten salt synthesis method different CCTO morphology (cube, polyhedron, nanorod and octahedron). They found that octahedron and nanorod morphologies exhibit the best behavior under visible light, attributed to the high abundant of oxygen vacancies on the surface. Since that the presence of Ti^{3+} enhances the photoelectrochemical and photocatalytic behaviors, thus several investigations focused on Ti^{3+} self-doped in TiO_2/ graphene composites in presence of reductant agent [25]–[28]. On the other hand, several works reported that presence of the CuO on the surface of TiO_2 photocatalyst not only enhance the adsorption of light in the visble regions, but also facilitates the separation of photogenerated electrons, and holes, and thus improving its photocatalytic activities [29], [30]. CuO is p-type semiconductor, which forms p–n heterojunction with n-type TiO_2 semiconductor this junction facilitates the separation of photogenerated electrons and holes required for good photocatalytic activity. Moreover, Jumpatam *et al.* [31] reported that the segregation of CuO at the grain boundaries of CCTO increases their electrical conductivity due to the hopping of charge carriers between $Cu^{+}\leftrightarrow Cu^{2+}$, $Cu^{3+}\leftrightarrow Cu^{2+}$, and $Ti^{3+}\leftrightarrow Ti^{4+}$ sites in CuO/CCTO composites.

In this work, CCTO photoelectrocatalysts were prepared using different amounts of graphene oxide (1, 3, and 6%) by a low cost and scalable approach. Graphene are known as 2D high surface materials, useful for fabricating inorganic composites due to their electronic property, high transparency, and flexible structure [32]. Partially oxidized graphene is favorable for its optical, conductive and chemical properties. The oxidized graphene is functionalized by

carboxylic acid, hydroxyl, and epoxide groups to form the graphene oxide (GO) [33]. GO materials could be insulating or conductive depending on the oxidation degree (C/O ratio) [34]. Furthermore, graphene oxide has been found to be either a p-type or n-type semiconductor [35]. Several investigations used modified graphene in inorganic composites for electronic, photoelectrocatalytic, and photocatalytic application have been reported [36], [37]. Graphene not only improve the photocatalytic activity of composite materials, but also could change the direction of grain growth during the consolidation composites powders [38]–[40]. Moreover, the oxidation of GO during sintering might result in the partial reduction of transition metals in oxide materials.

In this work, CCTO based composited were formed as pellets in one easy sintering step. The oxidation of GO at high temperature changes the electronic structure of CCTO materials and creates lattice defects and CuO segregation on the surface which enhances the photoelectrochemical behavior. Moreover, GO reduces the preferred orientations in the CCTO samples during the sintering process. The prepared materials were then fully characterized. The crystallinity and vibrational modes of the material were investigated using XRD and Raman spectroscopy. The morphology and element distribution were analyzed by scanning electron microscopy. X-ray Photoelectron Spectroscopy was employed to study the electronic structure of the materials. Optical properties were performed using PL and UV-Vis spectroscopies. Finally we evaluate electrochemical activities (cyclic and linear voltammetry) and the conductivity (impedance measurement) in dark and under visible light irradiation. The hydrogen production efficiency of these CCTO based materials was also investigated.

2. Experimental Section

2.1 Materials

Titanium (IV) Oxide (TiO_2- CAS Number: 13463-67-7, 99.5%), Potassium Hydroxide (KOH-CAS Number: 01900-20-08, ≥85%), Graphite (CAS Number: 7782-42-5, graphite pulver <20 Micron, synthetic), Sulfuric acid (H_2SO_4, CAS Number: 7664-93-9, 95-98%), Phosphoric acid (H_3PO_4, CAS Number: 7664-38-2, 99%), Potassium Permanganate ($KMnO_4$, CAS Number: 7722-64-7, 99.0%), Hydrolic acid (HCl, CAS Number: 7647-01-0, 36.2%), and Absolute Ethanol (CAS Number: 64-17-5, 99.94%) were purchased from Sigma Aldrich. Calcium Carbonate ($CaCO_3$-CAS Number: 471-34-1, 98%) and Copper (II) Oxide (CuO-CAS

Number: 1317-38-0, 98%) were purchased from Alfa Aesar. All chemicals were used without any further purification.

2.2. Synthesis of Graphene Oxide (GO)

Graphene oxide was synthesized from natural graphite powder, following modified Hummer's method [37], [41]. Briefly, 3g of graphite were dispersed in concentrated H_2SO_4:H_3PO_4 (9:1, 400 mL) solution. Then, 18 g of $KMnO_4$ were added gradually to the mixture and it was stirred for 12 h. Later on, the mixture was cooled down to room temperature and 3 mL of H_2O_2 were added. A brown precipitate was observed; showing that exfoliation of graphene oxide from graphite was being carried out. After one hour stirring, the GO was separated by centrifugation at 6000 rpm for 10 minutes and the supernatant was decanted away. The resultant precipitates were washed several times with 30% hydrochloric acid and absolute ethanol. Finally, the obtained powder was dried at 50°C for 24 hours to obtain the pure graphene oxide.

2.3 Preparation of $CaCu_3Ti_4O_{12}$ pellets

In an alumina jar (Al_2O_3), a stoichiometric amount of precursors (TiO_2 (1.56g), CuO (1.16g), and $CaCO_3$ (0.48g)) is mixed with alumina balls according to a defined ratio (precursors/ball = 1/9), in a ball milling machine for 5h. Then the mixture was calcined at 900°C for 3h to obtain CCTO powders. Powders are then pressed into a mold with 10 mm of diameter and 1-2 mm of thickness to form pellets using hydraulic press (3.5T) at room temperature. At the final step, the pellet was sintered at 1100°C for 3h.

2.4. Preparation of CCTO (1%GO), CCTO (3%GO), and CCTO (6%GO)

After powders calcination at 900°C for 3h, a phase of CCTO is obtained. CCTO powders were mixed using different amount (x) of graphene oxide (GO) (%x=1, 3, and 6%) using solid state method. The mixture was then molded into pellets (d=10 mm and e= 1-2 mm) using hydraulic press at 3.5T at room temperature. The as-prepared pellets finally were sintered at 1100°C for 3h to obtain CCTO (1%GO), CCTO (3%GO), and CCTO (6%GO) labeled as C1GO, C3GO, and C6GO respectively.

2.5 Characterizations of pellets

The crystalline phase of the obtained pellets was analyzed by X-ray diffraction (XRD), using a PANAlytical Xpert-PRO diffractometer equipped with an Xcelerator detector using Ni-

filtered Cu-radiation with wavelength of 1.54 A. The scan step size of all prepared pellets was fixed at 0.0167°/step and the time per step was 0.55 sec/step. Rietveld refinement was performed using the FULLPROF program and profile function 7 (Thompson-Cox-Hastings pseudo-Voigt convoluted with axial divergence asymmetry function) [42]. The morphology of all ceramics was studied via scanning electron microscopy (SEM), where images were taken with a Hitachi S4800, Japan. Elemental mapping were performed with a Zeiss EVO HD15 microscope coupled with an Oxford X-MaxN EDX detector. Raman spectra were measured by the dispersive Raman spectroscopy (Horiba XploRa, λ=659 nm), at a power of 20 W with the following acquisition conditions: continuous mode of 10 seconds, snapshot time of 7 seconds, numver of accumulations set to 30 times with a microspoce objective lens of 100x. In order to investigate the oxidation state of elements in pellets, X-ray photoelectron spectroscopy (XPS) was performed using XPS: monochromatic X-ray source: Al-Kalpha, 1486.6 eV - Resolution FWHM 0.45 eV.

Room temperature continuous wave (cw) Electron Paramagnetic Resonance (EPR) measurements at X-band frequencies (9.78 GHz) were conducted with a Bruker B-ER420 spectrometer upgraded with a Bruker ECS 041XG microwave bridge and a lock-in amplifier (Bruker ER023M) using a Bruker TE102 resonator applying a modulation amplitude of 5 G and a modulation frequency of 100 kHz. The samples were measured in quartz tubes of 2.9 mm outer diameter with a filling height of approx. 8.5 mm containing approx. 0.07-0.08 mg powdered sample.

The elemental analysis of carbon was performed in a Thermo FlashEA 1112 Elemental Analyzer (Thermo Fisher Scientific, Germany).

The band gab of pellets was measuring from UV–vis spectra. These spectra were measured by a UV–vis spectrophotometer (Jasco model V-570) equipped with a diffuse reflectance (DR) attachment (Shimadzu IRS-2200). Room temperature photoluminescence (PL) was measured in the range of 350–900 nm. After excitement with a nitrogen Nd:YAG laser (266 nm, 10 mW, 1 kHz), PL was recorded with an optical fiber spectrometer (Ocean Optics usb2000).

2.6. Electrochemical Measurement

Electrochemical measurements for oxygen evolution reaction (OER) were carried out in a three- electrode system using 1 M KOH as the electrolyte in dark and under visible light exposition using 150 W linear halogen lamp (the visible light source is in the range of 420-600 nm). CCTO and GO (x%)/CCTO pellets with a diameter of 10 mm was used as working electrode, Ag/AgCl as reference electrode and platinum wire as counter electrode.

Electrochemical Impedance spectroscopy measurements in dark and under visible light irradiation were performed at room temperature in the frequency range of 0.01Hz to 10^6 kHz with voltage bias of 20 mV amplitude.

The distance between the lamp and the quartz window was maintained at 10 cm. where, the power density was 8.2 mW/cm^2. For hydrogen evolution measurements, every 30 min gas sample was collected using a syringe to evaluate hydrogen and have been monitored by gas chromatography (Clarus-400, PerkinElmer, TCD (2mx1mm), He carrier).

Results and discussions

The obtained pellets were synthesized using mecanosynthesis method followed by sintering step at 1100°C for 3h. Pellets are formed from pure phase of CCTO and CCTO with different amount of graphene oxide (%x=1, 3, and 6%). The crystallinity and morphology of pellets are characterized by XRD, SEM, XPS and Raman. The optical properties were investigated using UV-Vis and photoluminescence measurements. Finally, in order to study the performance of obtained materials under visible light and their resistivity, electrochemical measurements (cyclic and linear voltammetry) and Electrochemical Impedance spectroscopy were performed in a system of three electrodes in 1M of KOH solution.

Physico-Chemical characterizations

XRD patterns of CCTO pellets, sintered at 1100°C for 3h without and using different weight ratio (x%) of GO (x=1, 3 and 6% of graphene oxide), were recorded in Figure 1. The XRD reflections in the measured patterns of all materials can be assigned to the cubic structure of $CaCu_3Ti_4O_{12}$ (space group *Im*-3) as a main phase and monoclinic CuO (space group *C*2/*c*) as minor phase. No additional XRD reflections attributed to GO or any of other crystalline carbon/carbides phases were observed in the XRD pattern of all materials, which suggests the oxidations of GO as well as any other carbon residuals at this high temperature. This result is in good agreement with elemental analysis measurements, which show the presence of negligible amount of carbon (< 0.01 at %) in all samples. It can be clearly seen that the intensities of XRD reflections corresponding to $CaCu_3Ti_4O_{12}$ phase differ slightly for different samples, suggesting preferred orientations of crystallites. Figure 1 b shows the intensities ratio of the (422) and (220) reflections for $CaCu_3Ti_4O_{12}$ phase in the four samples

in comparison with that of calculate pattern of $CaCu_3Ti_4O_{12}$ reference (PDF card #00-075-2188). $I_{CCTO(422)}/ I_{CCTO(220)}$ ratios for the CCTO and C6GO samples are much higher than that for the reference pattern, suggesting that the grains of the sintered CCTO and C6GO samples are preferentially grown along the [422] direction. In contrast, $I_{CCTO(422)}/ I_{CCTO(220)}$ ratios for C1GO and C3GO samples are very close to that of the reference pattern, which indicates the isotropic growth of the grains in these samples. These results are in consistent with previous results reported that graphene-based materials could change the direction of grain growth during the consolidation composites powders [38]–[40]. However, this effect of graphene-based materials is high at low content of graphene and decrease with increasing its amount in the composites due to the agglomeration of graphene, therefore, C6GO sample sintered using high GO content exhibits similar preferred orientation to that of CCTO sample. Moreover, these XRD reflections are shifted to lower two theta angles for the samples prepared using GO, indicating the increase in the lattice parameters of $CaCu_3Ti_4O_{12}$ phase in these samples. Rietveld refinement of XRD patterns confirmed this increase in lattice parameter *a* from 7.3914(1) Å for CCTO sample to 7.3922 (1), 7.3927 (1) and 7.3942 (1) Å for C1GO, C3GO and C6GO, respectively. This increase in the lattice parameter using GO during the sintering can be explained by the partial reduction of smaller cations such as Cu^{2+} and Ti^{4+} to larger Cu^{+} and Ti^{3+} during the oxidation process of GO. It has been reported that several transition elements can be reduced by CO oxidation [43], [44] that might be formed during the thermal oxidation of GO. The change in the cation stoichiometry of $CaCu_3Ti_4O_{12}$ could be another reason for this increase as the amount of the secondary CuO phase increased using GO nanosheets according to XRD analysis. As it can be seen in Figure 1, the intensities of XRD reflections corresponding to CuO phase are drastically changed with using GO during the sintering, indicating the change in the amount of CuO phase on the surface of sintered samples. As shown in Figure 1 b, the intensities ratio of the (111) reflection for CuO and (211) reflection for $CaCu_3Ti_4O_{12}$, which does not suffer from preferred orientation, increases for the samples sintered in the presence of GO materials. The highest amount of CuO is likely to be in C3GO sample. These results are in good agreement with previous studies showed that Cu deficiency and the partial reduction of Cu^{2+} and Ti^{4+} cations can lead to the expansion of CCTO phase [45]. This finding suggests that the samples sintered in the presence of GO may contain a defect-rich CCTO phase and high amount of CuO phase on the surface.

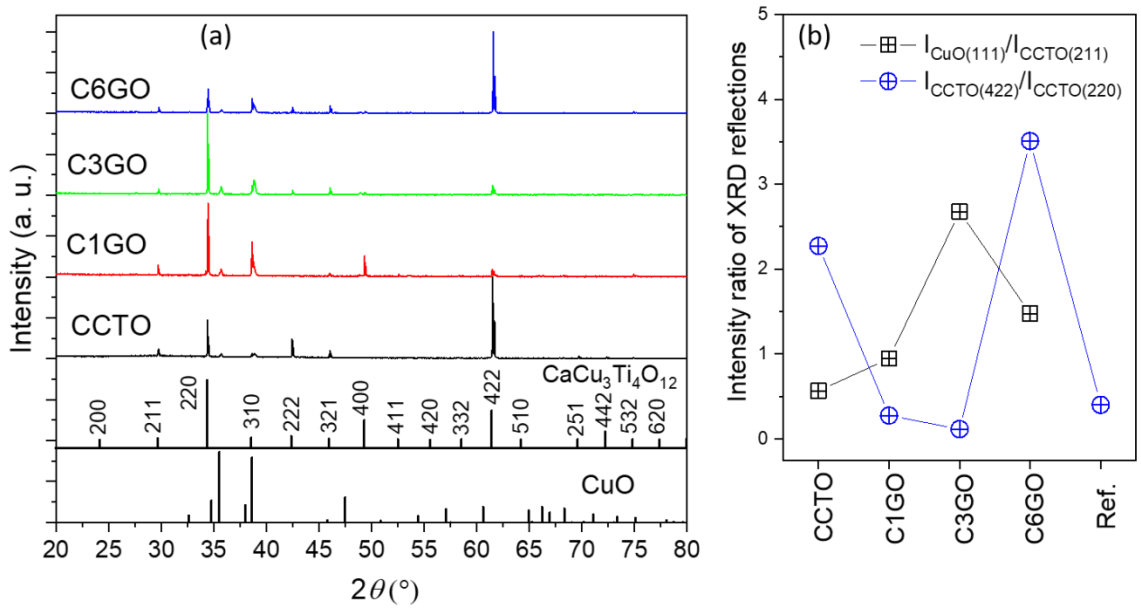

Figure 1 : (a) X-ray diffraction patterns of CCTO, C1GO, C3GO and C6GO ceramics sintered at 1100°C/3h. The calculated pattern of $CaCu_3Ti_4O_{12}$ (PDF card #00-075-2188) and CuO (PDF card #00-048-1548) are shown in the bottom. (b) The intensities ratio of some selected XRD reflections for CCTO, C1GO, C3GO and C6GO samples as well as $CaCu_3Ti_4O_{12}$ (PDF card #00-075-2188) for comparison.

Surface morphology of CCTO, C1GO, C3GO and C6GO are shown in Figure S1a, S1b, S1c and S1d respectively. It is clearly seen that grain and grain boundary growth change after adding different amounts of graphene oxide during the sintering process. The grains sizes are reduced progressively due to the addition of GO. Consequently, an increase in grain boundaries thickness was observed. In order to understand these results, SEM/EDX mapping has been performed on the surface of all pellets. As shown in Figure 2a, 2b and 2c corresponding to CCTO, C1GO and C3GO, all major elements (Ca, Cu, Ti and O) exist with a homogenous distribution. It is clearly seen that grain boundaries of all samples are Cu-rich and the amount of Cu content increases in the C1GO and C3GO samples sintered in the presence of GO material. These results suggests that using GO during sintering led to the formation of additional CuO phase on the grain boundaries, which is in accordance with XRD and SEM results.

The mechanism of formation of CuO phase on the grain boundaries during sintering can be explained as follows. Normally at around 950°C, the eutectic point of CuO-TiO_2 (liquid phase) appears at the surface of the materials. At this point, the atoms can migrate and diffuse

easily between grains and grain boundaries. Moreover, it has been reported that Cu^{2+} are not stable at high temperature and tend to be reduced to Cu^{+}, leading to a slight substitution of Ti^{4+} on Cu site for charge compensation [46]. Upon cooling, the Cu^{+} might donate electrons into the Ti 3d conduction band and convert back to Cu^{2+}, forming CuO phase. The location of CuO phase on the grain boundaries might be due to the migration of CuO phase to grain boundaries when cooling down, which is also reported in previous studies [31], [47]. As discussed above, the presence of GO material during sintering process facilitate the reduction of Cu^{2+} into Cu^{+} ions, thus, higher amount of CuO phase is observed in C1GO and C3GO samples in comparison with that in the CCTO sample.

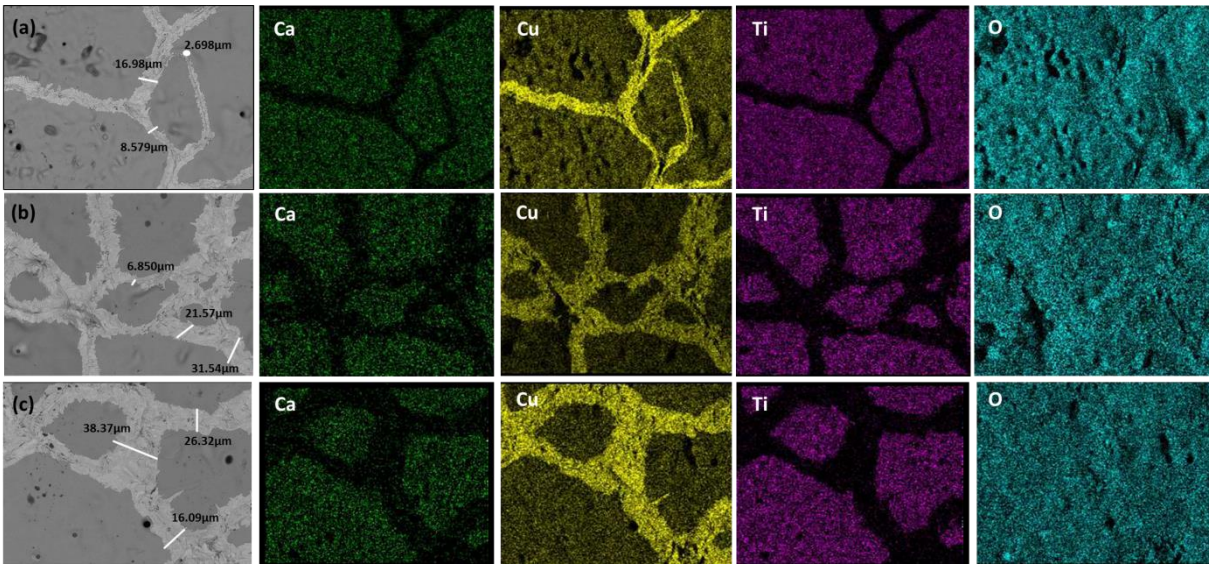

Figure 2 : SEM/EDX mapping of (a) CCTO, (b) C1GO and (c) C3GO ceramics.

High resolution X-ray photoelectron spectroscopy (XPS) analysis of CCTO, C1GO and C3GO materials has been investigated, to elucidate the elemental composition and chemical states of elements on the samples surface. As summarized in Table 1, the surface elemental composition calculated from XPS survey (Figure S2) was found to be Ca = 3.32 at. %, Cu = 6.94 at. %, Ti = 9.69 at.% and O = 78.52 at. % of CCTO sample, while the C3GO composite shows lower amounts of calcium (2.04 at. %), less oxygen (74.30 at. %) and a higher copper content (14.33 at. %), with similar titanium content (9.33 at. %). The atomic ratios of Cu/Ti and Cu/Ca were found to be increased with increasing the amount of used GO during sintering. These results are in the line with XRD and SEM/EDX results, which reveal the increase in the amount of CuO phase on the samples surface with increasing the amount of used GO nanosheets. Figure 3a, 3b, and 3c show the high resolution XPS spectra of O 1s, Cu

2p and Ti 2p, respectively. In Figure 3a the spectra of O 1s is shown, where four peaks are observed at arround 528.97, 530.55, 531.92 and 533.22 eV. The lower binding energy peaks at 528.97, 530.55 eV can be assigned to the oxygen lattice O^{2-} bonded to Cu^{2+} and Cu^{+} ions, respectively, the peak at 531.92 eV to O^{1-} or hydroxides and the higher binding energy peak at 533.22 eV to adsorbed oxygen (i.e. adsorbed H_2O), respectively [48]. On the other hand, the Cu 2p spectra can be fitted with four peaks, while, the Ti 2p spectra composed of two peaks, suggesting the presence of different valence states for Cu (Cu^{2+} and Cu^{+}) and Ti (Ti^{4+} and Ti^{3+}) on the surface [48]. These results are in good agreement with XRD results, which reveal the expansion of CCTO lattice due to the partial reduction of smaller Cu^{2+} and Ti^{4+} to larger Cu^{+} and Ti^{3+} during the oxidation process of GO. Moreover, in contrast to the Ti 2p spectra, remarkable changes in the O 1s and Cu 2p spectra were observed with increasing the used amount of GO during sintering, which could be explained by the change in the amount of CuO phase on the samples surface. The using of GO leads to CuO segregation at grain boundaries as seen in Figure 2b (SEM/EDX mapping), which mean the decomposition of CuO from CCTO lattice and thus creation of cation vacancies [31].

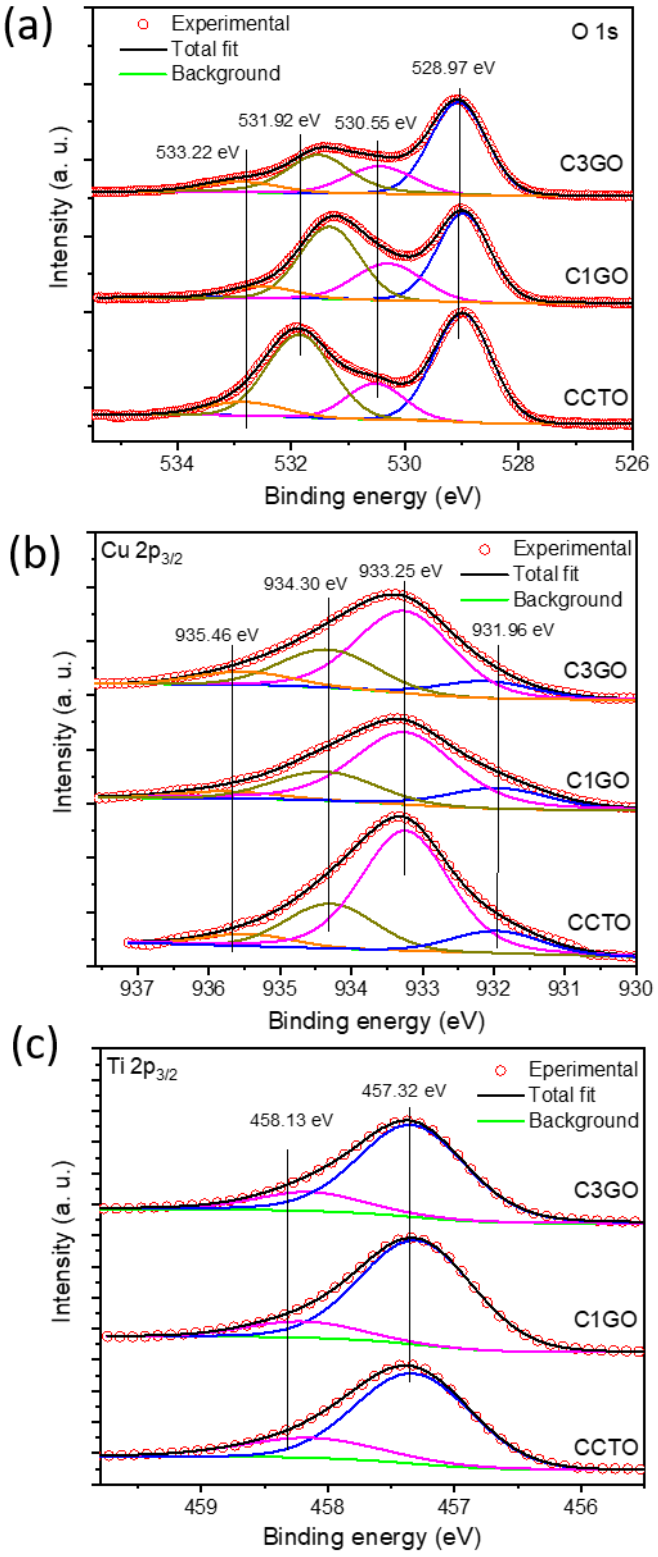

Figure 3 : High resolution XPS Spectra of (a) O1s, (b) Ti 2p, and (c) Cu 2p of CCTO, C1GO, and C3GO, ceramics

Table 1 : Atomic concentration of each constituent from the survey scans of CCTO, C1GO, and C3GO, ceramics

Sample	Ca (atom %)	Cu (atom %)	Ti (atom %)	O (atom %)	Cu/Ca	Cu/Ti
CCTO	3.32	6.94	9.69	78.52	2.09	0.72
C1GO	3.67	9.40	8.64	78.28	2.56	1.10
C3GO	2.04	14.33	9.33	74.30	7.02	1.54

The partial reduction of Ti^{4+} and Cu^{2+} is expected to be accompanied with the creation of oxygen vacancies in $CaCu_3Ti_4O_{12}$ lattice. However, the precise determination of oxygen vacancies in samples by fitting XPS spectra is very difficult. Therefore, room temperature continuous wave (cw) Electron Paramagnetic Resonance (EPR) measurements were performed on all samples. Figure 4 shows the cw EPR spectra of CCTO, C1GO, C3GO and C6GO samples normalized to the same peak to peak amplitude. The cw EPR spectra of all samples sintered in the presence of GO (C1GO, C3GO and C6GO) display a broad symmetric signal at $g \approx 2.15$ with a ΔB_{pp} linewidth of approx. 77 G of almost identical intensity. The spectra show no clear changes with varying GO content demonstrating that the detected spin system is not strongly affected by the GO concentration. For the CCTO sample sintered without using GO, the signal also detected at $g \approx 2.15$ exhibits an only slightly broader ΔB_{pp} linewidth of approx. 81 G suggesting an overall small effect of the presence of GO on the detected spin system. The broad signal of $CaCu_3Ti_4O_{12}$ was earlier ascribed to Cu^{2+} ions exhibiting antiferromagnetic ordering below 25 K [49], [50]. Previously, a significant increase in line width and intensity was attributed to the presence of paramagnetic oxygen vacancies [49], [50]. This effect is clearly not observed for the sintered samples with using GO investigated in this study. These samples rather exhibit a slight decrease in ΔB_{pp} linewidth compared to the CCTO sample indicating rather reduced spin interaction assuming a homogeneous line broadening. However, it should be noted that a change in the presence or number of oxygen vacancies cannot be fully excluded by these EPR measurements, as changes in the spectra due to a small number of oxygen vacancies, e.g. in a thin surface layer, may be obscured by the intense Cu^{2+} signal.

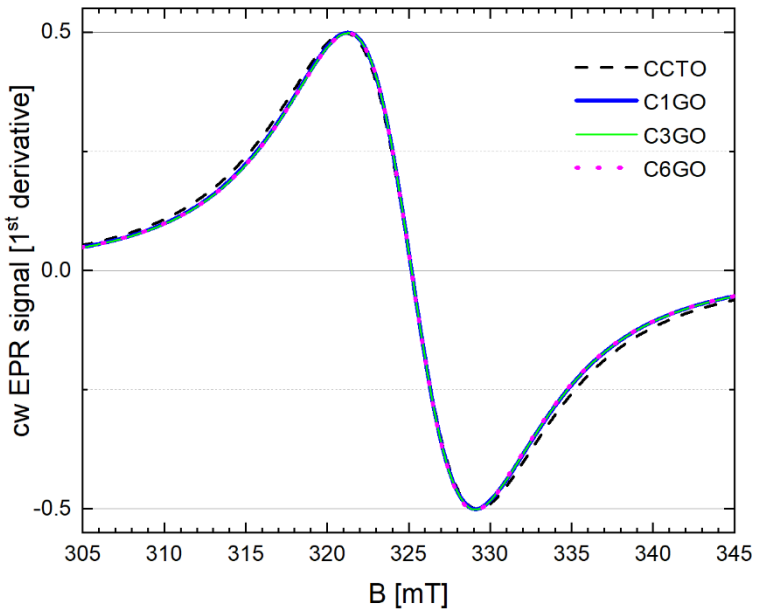

Figure 4 : Room temperature cw EPR spectra of samples C1GO, C3GO, C6GO and CCTO as reference, normalized to amplitude (9.8 GHz, 5 G, 100 kHz, 2 mW mw power)

Micro-Raman spectroscopy is used to determine vibrational modes of molecules. In this part, Micro-Raman is used to investigate the effect of using GO nanosheets on the crystal structure of CCTO materials. Acccording to the litterature, CCTO exhibit three main active bands in Raman spectroscopy at 445, 506 and 570 cm^{-1} [51]. Raman spectroscopy for CCTO, C1GO, C3GO and C6GO is recorded between 100 and 600 cm^{-1} on grain and grain boundaries in Figure 5i and 5ii respectively.

Figure 5i presents Raman band on grains and it showed the three main band related to TiO_6 clusters (modes P7, P8 and P9 corresponding to 445, 506, and 570 cm^{-1} respectively). P7 and P8 modes appeared at high intensity, refer to TiO_6 clusters (Ag symmetrie), the third mode (P9) corresponding to Ti-O-Ti antistretshing (Fg symmetrie) mode is present at very low intensity but it increases slightly after adding graphene oxide, maybe due to the changement in the amount of polarization states [52]. From Figure 5ii, it can be seen that CuO modes appear at high intenisty which confirms that CuO phase is located at the grain boundaries. P7 and P8 modes appears for C3GO material at low intesity which could be explained due to the grain boudaries growth on grain regions. The oxidation of GO and the presence of Cu element on grain boundaries (as seen below in Figure 5ii) results a monovalent copper for charge compensation [53].

The slight shift of Raman modes corresponding to the CuO phase for C3GO and C6GO samples might be due to the stress and/or non-stoichiometry in the CuO formed in grain boundaries [54]. It is known that D and G modes characteristic of GO appear at arround 1350 cm^{-1} and 1600 cm^{-1} rescpectively [55]. In our study these two modes do not exist due to the approximately total oxidation of GO at 1100°C, which agrees with the results of carbon elemental anylysis.

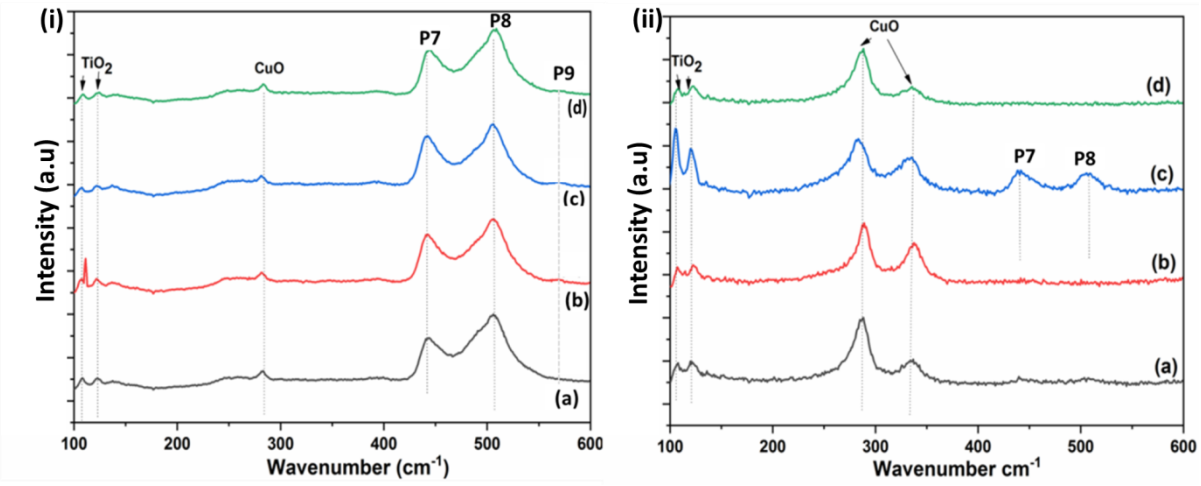

Figure 5 : Raman shifts on i) grains and ii) grain boundaries of (a) CCTO, (b) C1GO, (c) C3GO and (d) C6GO pellets.

Optical properties

In order to investigate the effect of defects made in CCTO materials as result of GO oxidation, on the optical band gap, UV–Vis diffuse reflectance measurements were performed. Figure 6 showed two absorbance bands at around 1.6 and 2.9 eV corresponding to the hybridized valence band (VB) Cu 3d-O2p and to the conduction band (CB) Ti-3d states respectively [24]. The optical band gap E_g of the samples was determined (Figure 6a) by Kubelka-Munk remission function according to the following equation (eq. 1)

$$\alpha h\nu^{1/2} = A(h\nu - E_g) \qquad \textbf{Equation 1}$$

Where α is the absorption coefficient, ν is light frequency and E_g is an direct transition band gap. The E_g obtained values (Figure 6b) are 3.46, 3.43, 3.42 and 3.41 eV corresponding to CCTO, C1GO, C3GO and C6GO respectively. This little decrease of the band gap energy can be related to the crystallinity or the formation of electronic energy levels within energy band

gap [56], [57]. In our study crystallite sizes did not vary between different materials even after using GO, thus the first reason can be discarded. Therefore, forming mid band gap energy levels in materials sintered in the presence of GO might be due to the partial reduction of Ti^{4+} to Ti^{3+}, accompanied with the segregation of Cu from CCTO lattice, for charge compensation. The electronic transition from valence band to oxygen level then to Ti^{3+} then to conduction band cause a red shift in adsorption edge showing reduced band gap [58]. The intensity of absorbance band increases after adding GO due to the presence of CuO (Cu^{2+}) and the active species (Ti^{3+}) [59]. The obtained values of CuO band gap are calculated as seen in Table S1 and Figure S3.

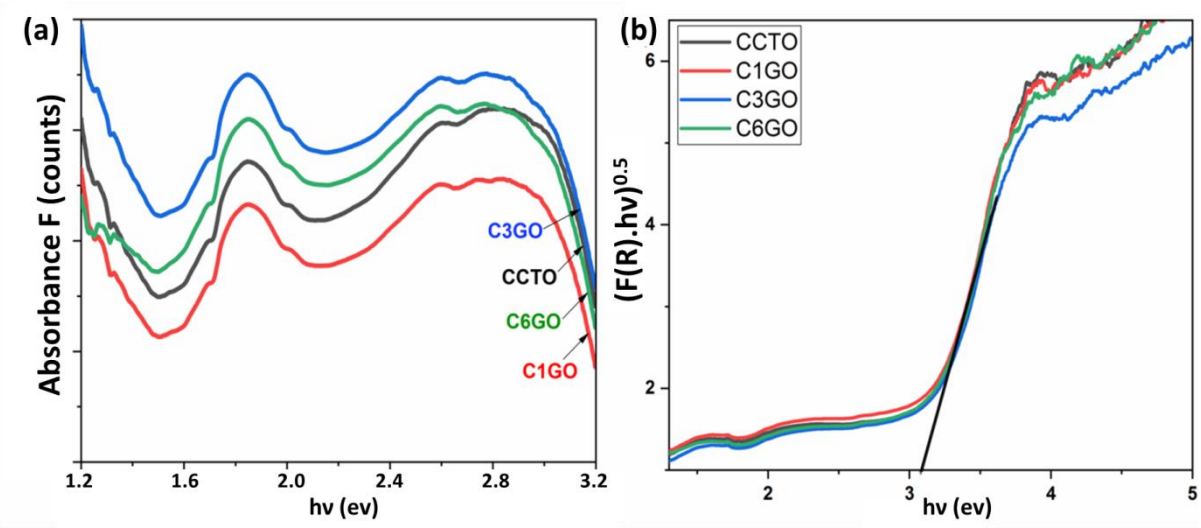

Figure 6 : (a) Reflectance spectra and (b) Band gap calculation from reflectance spectra of CCTO, C1GO, C3GO and C6GO

The photoluminiscence measurements were used to be correlated with electronic and structural properties of oxides [60]. PL spectra of CCTO, C1GO, C3GO and C6GO materials at room temperature are shown in Figure 7. Similar spectra shape indicates the same electronic band structure for all materials. UV part of emission spectra shows band-to-band transitions in TiO_2 (peak, centered at 385 nm). Forming of the composites results in charge separation and reduction of electron-hole pairs which participate in emission or/and new surface states are formed to realize an irradiative recombination. This UV emission can be attributed to recombination of the free excitons or near band edge emission of $CaCu_3Ti_4O_{12}$ because the PL emissions, relating to defects such as oxygen vacancies in $CaCu_3Ti_4O_{12}$, is usually appears in the visible light region [61]–[63]. This finding is supported by the XPS and

EPR results as discussed before. The slight decrease of PL intensity for CCTO and C6GO samples in comparison with that for C1GO and C3GO samples might be due to the strong preferred orientation in these two samples along the [422] directions as revealed by XRD analysis. As shown in Figure 1 b, the highest preferred orientation was observed for C6GO samples, thus, it shows the lowest PL intensity (Figure 7). This orientation effect on the PL behaviour has been reported for many other semiconductor oxides and it can be attributed to the different disorder or defects located at different crystal planes [64]. Therefore, C1GO and C3GO samples show high PL intensities due to the isotropic growth of their grains (Figure 1 b).

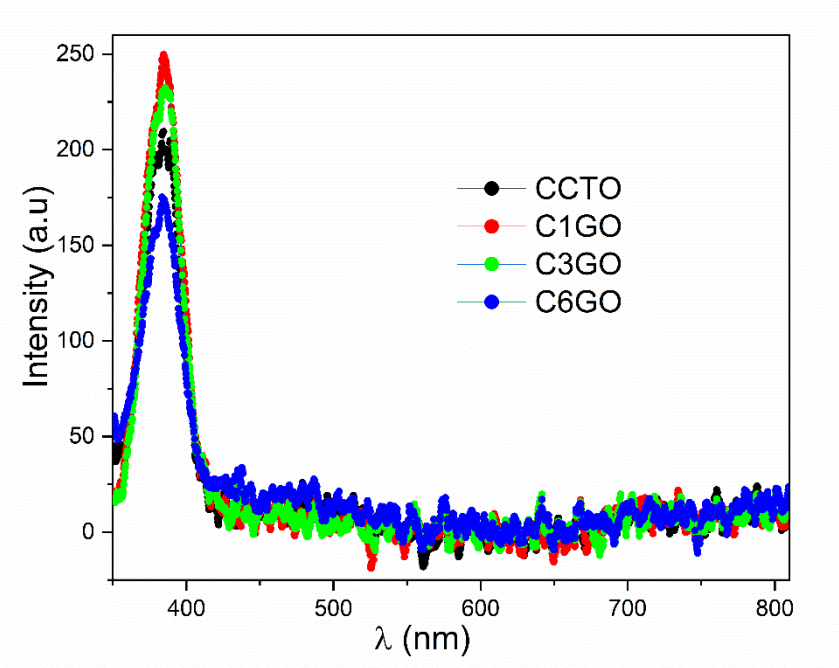

Figure 7 : Photoluminescence spectra of pure CCTO, C1GO, C3GO, and C6GO

Electrochemical behavior

CCTO pellets prepared using different amounts of GO are used as electrodes in 1M KOH solution to investigate their photoelectrochemical behavior. CCTO prepared without and with GO were considered as working eletrode, Pt as counter electrode and Ag/AgCl as a reference. Cyclic voltammetry curves are recorded in Figure 8. Figure 8a shows CV curves for the different samples between 1 V and 2.4 V in oxygen evolution range (OER range vs Ag/AgCl). CCTO material in dark (d-CCTO) seems inactive as seen from Figure 8a. After light exposition, the activity of CCTO is enhanced and start to generate photocurrent. It is clear that

the generation of current increase for the samples prepared with GO in dark and under visible light exposition. There is no hysteris form due to that for voltages higher than 1.6 V, the resistivity of materials increases. It may be related to the formation of an insulator layer on surface defects at high voltage. The electrochemical activity of these materials prepared with GO still poor with no sigificant difference except for C3GO materials.

CCTO prepared with 3% of graphene oxide is electrochemically active in dark (d-C3GO) and under visible light exposition (v-C3GO) (Figure 8b). The photoelectrochemical behavior for CCTO pellets depend largely on the surface properties. Different activities of these CCTO based materials is related to surface properties. For example, it has been reported that oxygen vacancies, Cu^{+} and Ti^{3+} on the surface of $CaCu_3Ti_4O_{12}$ could improve the visible light absorption and reduce the carrier recombination, which improve photocatalytic activity of $CaCu_3Ti_4O_{12}$ [24]. However, XPS, EPR, Raman and PL results revealed that all samples might have a small amount of oxygen vacancies, which suggests that other reasons could be responsible for the better activity of C3GO sample. XRD, SEM/EDX and XPS results showed that C3GO sample has isotropic grain domains with highest amount of CuO in the grain boundaries. Thus, this high amount of CuO on the surface might be the reason for enhancing the photoelectrochemical behaviour of C3GO sample in comparison to other materials. The CuO on the CCTO surface not only increases the adsorption of light in the visible regions, but also facilitates the separation of photogenerated electrons, and holes, and thus enhancing the photocatalytic activities of the composites [29], [30]. It has been reported that combining CuO, p-type semiconductor, with n-type semiconductor material such as TiO_2 might form a p–n heterojunction in the composite [29], [30]. The photogenerated holes migrate from p-type to n-type region, while, electrons move from n-type to p-type region within the junction, resulting in an electric field at equilibrium. Thus, photogenerated electrons and holes can be separated by moving back to the conduction band of the n-type TiO_2 and the valence band of the p-type CuO, respectively. Since CCTO is n-type with a quite similar band gap to TiO_2, similar mechanism could be the reason for the higher photoelectrochemical behaviour of C3GO sample.

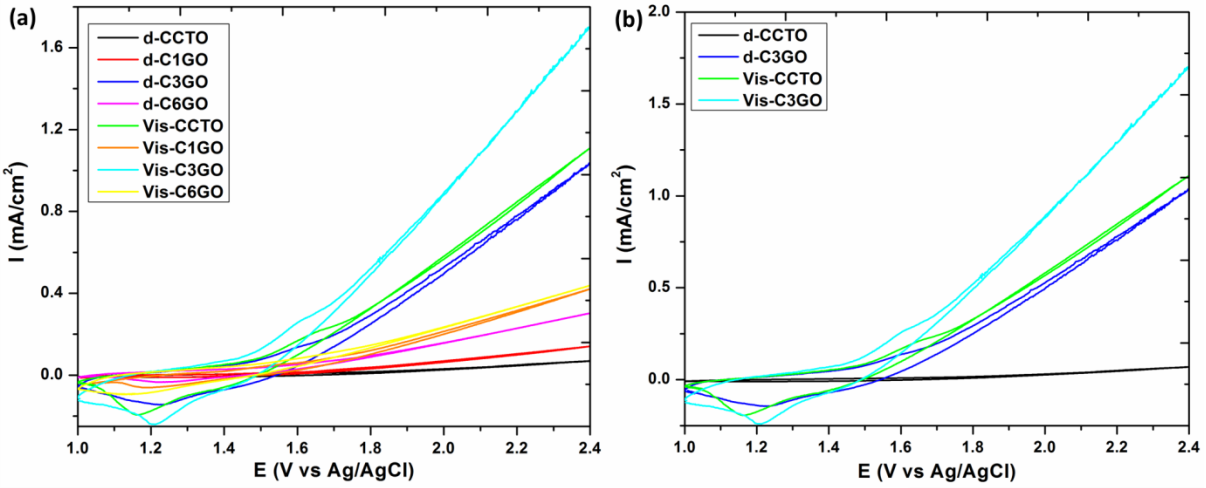

Figure 8 : CV curves in (a) OER range for CCTO, C1GO, C3GO, and C6GO, and (b) OER range of CCTO, and C3GO, in dark and under visible light. (In 1M KOH vs Ag/AgCl)

To demonstrate the enhanced electron transfer in active materials, the photoelectrochemical activity of materials in dark and under visible light was analyzed by measuring the photocurrent, using linear sweep voltammetry (LSV- Figure S4). The high photocurrent value indicates a strong capacity to generate and transfer photogenerated charge carries and thus enhance the photoelectrochemical activity [65]. In dark, the current density for CCTO and C3GO is recorded at an onset potential of 0.01 $A.cm^{-2}$ and 0.25 $A.cm^{-2}$ (Figure S4). After visible light exposition, the photocurrent generation from C3GO increases by 50% in comparison to CCTO. The photocurrent increase in two ranges with increasing bias voltage, indicates that the photoinduced electron-hole-recombination is embeded to accelerate electrons transfer [65].

Table 2 presents the photocurrent density of various materials with reactive species Ti^{3+} and Cu^{+} investigated in different electrolytes and using different sources of visible light. This table demonstrated the good performance of our material in comparison to what has been reported before.

Table 2 : Represents the photocurrent density of various studied materials

Materials	Photocurrent density (mA/cm^2)	Potential (V)	Light sources	References
TiO_2-22h	**1.4 mA/cm^2 in 1M KOH**	**0.9 vs. Ag/AgCl**	**300 W-Xe lamp**	[66]
0.2-RGO/TiO_{2-x}	**0.25 mA/cm^2 in 0.1M Na_2SO_4**	**0.9 vs. Ag/AgCl**	**500 W-Xe arc lamp**	[67]

MWR-TiO_2 NTPs	**2 mA/cm^2 in 1M KOH**	**0.9 vs. Ag/AgCl**	**AM 1.5G illumination (100mW/cm^2)**	[68]
Cu_2O/TiO_2-Cu^+	**0.6 mA/cm^2 in 3M NaCl**	**0.9 vs. Ag/AgCl**	**100 mW/cm (using LS 150 with AM1.5 G filter, Abet Technologies)**	[69]
3%wt.BN/CCTO	**3.6 mA/cm^2 in 1M KOH**	**0.9 vs. Ag/AgCl**	**150 W halogen lamp**	[70]
C3GO	**1.5 mA/cm^2 in 1M KOH**	**0.9 vs. Ag/AgCl**	**150 W halogen lamp**	**This work**

Electrochemical impedance spectroscopy (EIS) is used to study the resistivity of CCTO based materials. Figure S5a, S5b and S5c presents the Impedance spectra of these materials in dark and visible light for 0.4 V, 0.5 V and 0.6 V Vs Ag/AgCl reference electrode in 1M KOH solution. CCTO is caracterised by two semi circles one at high frequency corresponding to grain boundaries and the second at low frequency corresponding to grains (Figure 9). Which mean that the rate of charge transfer for photoelectrocatalytic acitivity is depending on the grains and grain boundaries behavior. The seperation of photogenerated hole-electron is an important step for semiconductor in order to improve photocatalytic and photoelectrocatalytic performances. The smallest arc radiuses refered to all material under visible light exposition leading to high rate of charge transfer thus higher the efficiency of charge separation [71], [72]. Therefore, the enhanced photocatalytic performance is mainly attributed to the increase of the charge separation efficiency due to the presence of CuO segregation at grain boundaries. It is debated in the literature that surface defects could be on CuO phase due to the generation of active species. In addition the redox activity of the CuO nanoparticles has a critical role to enhance the oxidation mechanism [73], [74]. Those electrons are trapped in CCTO lattice in mid gap states as Ti^{3+} ions, known as superficial donors of conduction electrons.

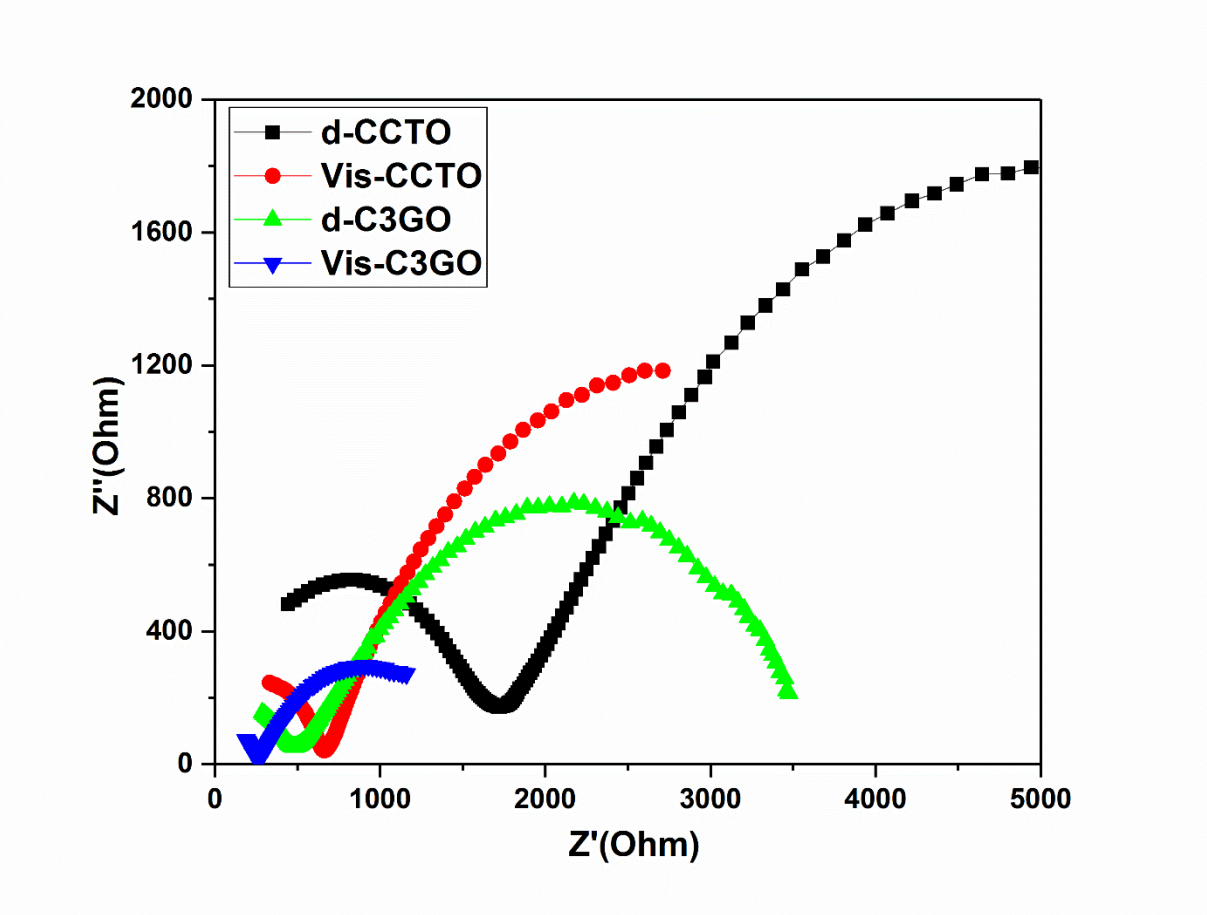

Figure 9 : The Nyquist plot of CCTO, C1GO, C3GO, and C6GO ceramics in dark and under visible light irradiation 0.5 V vs Ag/AgCl.

For quantitative measurement, plots of electrochemical impedance spectroscopy were fitted to the model of an equivalent circuit (Figure 10). In the model of Figure 10, R_1 is the resistance of electrolyte (1M KOH solution). The parallel combination of the interfacial charge transfer resistance (Rtc_2 and Rtc_3 resistance of the charhe transferd in grains boundaries and grain regions respectively) and the constant phase element (CPE) is also included in this circuit. The CPE instead of a capacitor is taken in consideration for frequency dispersion. Rtc_2 and Rtc_3 values are mentioned in Table 3. As shown in Table 3, the Rtc_2 resistance of the grain boundaries in the CCTO based materials is much lower than Rtc_3 of corresponding grain domains, which could be explained by the accumulation of CuO phase at the grain boundaries. This result agrees with previous work showed that the segregation of CuO at the grain boundaries of CCTO reduced the Rtc_2 resistance due to the hopping of charge carriers between $Cu^{+}\leftrightarrow Cu^{2+}$, $Cu^{3+}\leftrightarrow Cu^{2+}$, and $Ti^{3+}\leftrightarrow Ti^{4+}$ sites in CuO/CCTO composites [36].

Moreover, the resistivity of all samples decreases under visible light exposition thus leading to higher charge conductivity.

Table 3 : ***Electrochemical impedance spectroscopy parameter in all CCTO based materials***

	R_{tc2} (Ohm)		R_{tc3} (Ohm)	
	Dark	**Visible**	**Dark**	**Visible**
CCTO	**1861±5.05**	**743.2±16.81**	**7475±4.681**	**4401±16.56**
C1GO	**5131±63.43**	**1134±3.02**	**10443±39.51**	**4672±1.78**
C3GO	**1468±227.3**	**389.3±88.15**	**3483±2.447**	**1316±4.108**
C6GO	**1155±5.04**	**940.7±5.49**	**2528±1.812**	**1353±0.84**

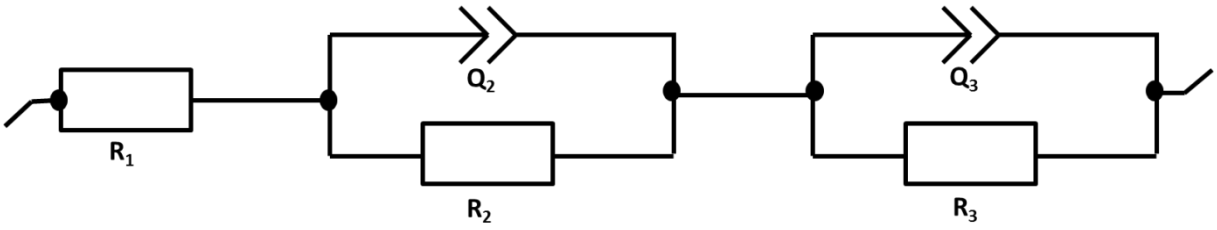

Figure 10 : EIS equivalent circuit for the impedance behavior

Hydrogen Evolution

Hydrogen generation (Figure 11a) has been performed for two hours using CCTO and C3GO as working electrode in order to test their efficiency. From Figure 12, it can be seen that the rate of hydrogen yield increases after adding 3%wt. of graphene oxide to CCTO. It is 50% (2.9 μmol/h) higher than the rate of hydrogen generation using CCTO on working electrode. C3GO presents the higher photocurrent density generation in comparison to CCTO as seen from LV measurement under visible light exposition. The average faradaic efficiency values were estimated to be around 73% and 79% for CCTO and C3GO respectively. The enhancement in faradaic values could be attributed to the decrease of the transfer charge in C3GO under visible light exposure as already seen from EIS measurements (Figure 10).

To evaluate the durability of the C3GO sample (Figure S6), the hydrogen production by photoelectrochemical experiments was performed in four cycles where each cycle lasts for 2 h as shown in Figure 11b the hydrogen production was linear and stable during these cycles.

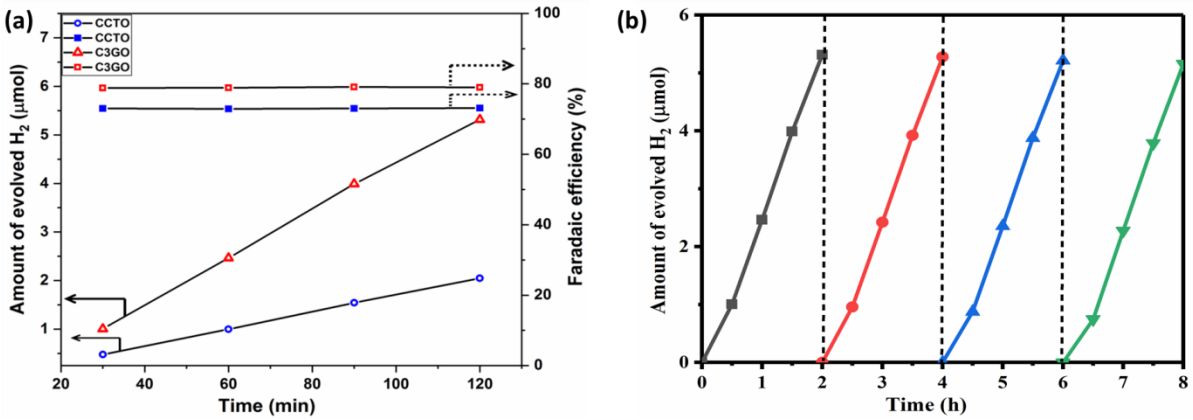

Figure 11 : (a) The faradaic efficiency and quantity of detected hydrogen derived from the CCTO (blue symbols) and C3GO (red symbols) and (b) Reusability of C3GO ceramics for photoelectrochemical H_2 production activity under visible light.

Conclusion

The oxidation of graphene oxide nanosheets in CCTO at high temperature induces surface modifications. In this work $CaCu_3Ti_4O_{12}$ based materials were prepared using different amounts of graphene oxide (1, 3, and 6%). Cubic perovskite phase of CCTO was observed for all materials with the presence of small amount of CuO as second phase. XRD analysis showed an increase in CuO amount using different % of GO in CCTO and as a result a slight increase in the lattice parameter due to the partial reduction of Cu^{2+} and Ti^{4+} cations in CCTO lattice as confirmed by XPS characterization. Thus, the oxidation of GO nanosheets at high temperature enhances the segregation of CuO on grain boundaries as detected by EDX mapping, XPS and Raman spectroscopy. Electrochemical measurement was performed in 1M KOH solution in dark and under visible light exposition and showed an increase by 50% of photocurrent generation recorded for C3GO in comparison to CCTO under visible light irradiation. Furthermore, electrochemical impedance spectroscopy showed that the resistance of the transferred charges decreases for the samples prepared with GO and under exposure to visible light due to the presence of active species (Cu^{+} and Ti^{3+}) on CCTO surface and CuO on grain boundaries. The hydrogen generation yield was determined and the obtained results demonstrated that H_2 rate increases to 2.9 µmol/h for the sample prepared using 3%wt. of GO which is 50% higher than the rate of hydrogen generation using pure CCTO.

References

[1] S. J. A. Moniz, S. A. Shevlin, D. J. Martin, Z.-X. Guo, and J. Tang, "Visible-light driven heterojunction photocatalysts for water splitting – a critical review," *Energy Environ. Sci.*, vol. 8, no. 3, pp. 731–759, 2015.

[2] A. Kudo and Y. Miseki, "Heterogeneous photocatalyst materials for water splitting," *Chem. Soc. Rev.*, vol. 38, no. 1, pp. 253–278, 2009.

[3] H. Ishaq, I. Dincer, and G. F. Naterer, "Performance investigation of an integrated wind energy system for co-generation of power and hydrogen," *Int. J. Hydrogen Energy*, vol. 43, no. 19, pp. 9153–9164, 2018.

[4] R. Łukajtis *et al.*, "Hydrogen production from biomass using dark fermentation," *Renew. Sustain. Energy Rev.*, vol. 91, pp. 665–694, 2018.

[5] T. Hisatomi and K. Domen, "Reaction systems for solar hydrogen production via water splitting with particulate semiconductor photocatalysts," *Nat. Catal.*, vol. 2, no. 5, pp. 387–399, 2019.

[6] Y. Lu *et al.*, "Self-hydrogenated shell promoting photocatalytic H2 evolution on anatase TiO2," *Nat. Commun.*, vol. 9, no. 1, p. 2752, 2018.

[7] W. Q. Zaman, W. Sun, Z. Zhou, Y. Wu, L. Cao, and J. Yang, "Anchoring of IrO2 on One-Dimensional Co3O4 Nanorods for Robust Electrocatalytic Water Splitting in an Acidic Environment," *ACS Appl. Energy Mater.*, vol. 1, no. 11, pp. 6374–6380, Nov. 2018.

[8] X. Li *et al.*, "Light Illuminated α−Fe2O3/Pt Nanoparticles as Water Activation Agent for Photoelectrochemical Water Splitting," *Sci. Rep.*, vol. 5, p. 9130, Mar. 2015.

[9] M. Zhang, J. Chen, H. Li, P. Cai, Y. Li, and Z. Wen, "Ru-RuO2/CNT hybrids as high-activity pH-universal electrocatalysts for water splitting within 0.73 V in an asymmetric-electrolyte electrolyzer," *Nano Energy*, vol. 61, pp. 576–583, 2019.

[10] Y. Che *et al.*, "Bio-inspired Z-scheme g-C3N4/Ag2CrO4 for efficient visible-light photocatalytic hydrogen generation," *Sci. Rep.*, vol. 8, no. 1, p. 16504, 2018.

[11] S. Mahzoon, S. M. Nowee, and M. Haghighi, "Synergetic combination of 1D-2D g-C3N4 heterojunction nanophotocatalyst for hydrogen production via water splitting under visible light irradiation," *Renew. Energy*, vol. 127, pp. 433–443, 2018.

[12] L. Shen *et al.*, "Black TiO2 nanobelts/g-C3N4 nanosheets Laminated Heterojunctions with Efficient Visible-Light-Driven Photocatalytic Performance," *Sci. Rep.*, vol. 7, p. 41978, Feb. 2017.

[13] H.-Y. Wang, Y.-Y. Hsu, R. Chen, T.-S. Chan, H. M. Chen, and B. Liu, "Ni3+-Induced Formation of Active NiOOH on the Spinel Ni–Co Oxide Surface for Efficient Oxygen Evolution Reaction," *Adv. Energy Mater.*, vol. 5, no. 10, p. 1500091, May 2015.

[14] H. Yang, F. Hu, Y. Zhang, L. Shi, and Q. Wang, "Controlled synthesis of porous spinel cobalt manganese oxides as efficient oxygen reduction reaction electrocatalysts," *Nano Res.*, vol. 9, no. 1, pp. 207–213, 2016.

[15] J. G. Lee *et al.*, “A New Family of Perovskite Catalysts for Oxygen-Evolution Reaction in Alkaline Media: BaNiO3 and BaNi0.83O2.5,” *J. Am. Chem. Soc.*, vol. 138, no. 10, pp. 3541–3547, Mar. 2016.

[16] W. T. Hong *et al.*, “Charge-transfer-energy-dependent oxygen evolution reaction mechanisms for perovskite oxides,” *Energy Environ. Sci.*, vol. 10, no. 10, pp. 2190–2200, 2017.

[17] D. Chen *et al.*, “Preferential Cation Vacancies in Perovskite Hydroxide for the Oxygen Evolution Reaction,” *Angew. Chemie Int. Ed.*, vol. 57, no. 28, pp. 8691–8696, Jul. 2018.

[18] M. A. Subramanian, D. Li, N. Duan, B. A. Reisner, and A. W. Sleight, “High Dielectric Constant in ACu3Ti4O12 and ACu3Ti3FeO12 Phases,” *J. Solid State Chem.*, vol. 151, no. 2, pp. 323–325, May 2000.

[19] J. H. Clark *et al.*, “Visible Light Photo-oxidation of Model Pollutants Using CaCu3Ti4O12: An Experimental and Theoretical Study of Optical Properties, Electronic Structure, and Selectivity,” *J. Am. Chem. Soc.*, vol. 133, no. 4, pp. 1016–1032, Feb. 2011.

[20] M. Mizumaki, T. Saito, H. Shiraki, and Y. Shimakawa, “Orbital Hybridization and Magnetic Coupling of the A-Site Cu Spins in CaCu3B4O12 (B = Ti, Ge, and Sn) Perovskites,” *Inorg. Chem.*, vol. 48, no. 8, pp. 3499–3501, Apr. 2009.

[21] H. S. Kushwaha, A. Halder, P. Thomas, and R. Vaish, “CaCu3Ti4O12: A Bifunctional Perovskite Electrocatalyst for Oxygen Evolution and Reduction Reaction in Alkaline Medium,” *Electrochim. Acta*, vol. 252, pp. 532–540, 2017.

[22] H. S. Kushwaha, N. A. Madhar, B. Ilahi, P. Thomas, A. Halder, and R. Vaish, “Efficient Solar Energy Conversion Using CaCu3Ti4O12 Photoanode for Photocatalysis and Photoelectrocatalysis,” *Sci. Rep.*, vol. 6, p. 18557, Jan. 2016.

[23] W. Yang *et al.*, “Oxygen vacancies confined in ultrathin nickel oxide nanosheets for enhanced electrocatalytic methanol oxidation,” *Appl. Catal. B Environ.*, vol. 244, pp. 1096–1102, May 2019.

[24] R. Hailili *et al.*, “Oxygen vacancies induced visible-light photocatalytic activities of CaCu3Ti4O12 with controllable morphologies for antibiotic degradation,” *Appl. Catal. B Environ.*, vol. 221, pp. 422–432, Feb. 2018.

[25] F. Zuo, L. Wang, T. Wu, Z. Zhang, D. Borchardt, and P. Feng, “Self-Doped Ti3+ Enhanced Photocatalyst for Hydrogen Production under Visible Light,” *J. Am. Chem. Soc.*, vol. 132, no. 34, pp. 11856–11857, Sep. 2010.

[26] Y. Ji *et al.*, “Surface Ti3+/ Ti4+ Redox Shuttle Enhancing Photocatalytic H2 Production in Ultrathin TiO2 Nanosheets/CdSe Quantum Dots,” *J. Phys. Chem. C*, vol. 119, no. 48, pp. 27053–27059, Dec. 2015.

[27] J. Pan *et al.*, “The enhancement of photocatalytic hydrogen production via Ti3+ self-doping black TiO2/g-C3N4 hollow core-shell nano-heterojunction,” *Appl. Catal. B Environ.*, vol. 242, pp. 92–99, 2019.

[28] H. H. El-Maghrabi, E. A. Nada, F. S. Soliman, Y. M. Moustafa, and A. E.-S. Amin,

"One pot environmental friendly nanocomposite synthesis of novel TiO2-nanotubes on graphene sheets as effective photocatalyst," *Egypt. J. Pet.*, vol. 25, no. 4, pp. 575–584, 2016.

[29] D. Lu, O. A. Zelekew, A. K. Abay, Q. Huang, X. Chen, and Y. Zheng, "Synthesis and photocatalytic activities of a CuO/TiO 2 composite catalyst using aquatic plants with accumulated copper as a template," *RSC Adv.*, vol. 9, no. 4, pp. 2018–2025, 2019.

[30] J. Bandara, C. P. K. Udawatta, and C. S. K. Rajapakse, "Highly stable CuO incorporated TiO2 catalyst for photocatalytic hydrogen production from H2O," *Photochem. Photobiol. Sci.*, vol. 4, no. 11, pp. 857–861, 2005.

[31] J. Jumpatam *et al.*, "Improved giant dielectric properties of CaCu3Ti4O12 via simultaneously tuning the electrical properties of grains and grain boundaries by F− substitution," *RSC Adv.*, vol. 7, no. 7, pp. 4092–4101, 2017.

[32] V. Thangaraj *et al.*, "Fluorescence Quenching of Sulfo-rhodamine Dye over Graphene Oxide and Boron Nitride Nanosheets," *Eur. J. Inorg. Chem.*, vol. 2016, no. 13-14, pp. 2125–2130, May 2016.

[33] X. Zhou *et al.*, "In Situ Synthesis of Metal Nanoparticles on Single-Layer Graphene Oxide and Reduced Graphene Oxide Surfaces," *J. Phys. Chem. C*, vol. 113, no. 25, pp. 10842–10846, Jun. 2009.

[34] D. W. Boukhvalov and M. I. Katsnelson, "Modeling of Graphite Oxide," *J. Am. Chem. Soc.*, vol. 130, no. 32, pp. 10697–10701, Aug. 2008.

[35] X. Wu, M. Sprinkle, X. Li, F. Ming, C. Berger, and W. A. de Heer, "Epitaxial-Graphene/Graphene-Oxide Junction: An Essential Step towards Epitaxial Graphene Electronics," *Phys. Rev. Lett.*, vol. 101, no. 2, p. 26801, Jul. 2008.

[36] S. Khamlich, Z. Abdullaeva, J. V Kennedy, and M. Maaza, "High performance symmetric supercapacitor based on zinc hydroxychloride nanosheets and 3D graphene-nickel foam composite," *Appl. Surf. Sci.*, vol. 405, pp. 329–336, 2017.

[37] S. Nagarajan *et al.*, "Porous Gelatin Membrane Obtained from Pickering Emulsions Stabilized by Graphene Oxide," *Langmuir*, vol. 34, no. 4, pp. 1542–1549, Jan. 2018.

[38] M. Rashad *et al.*, "Improved strength and ductility of magnesium with addition of aluminum and graphene nanoplatelets (Al+GNPs) using semi powder metallurgy method," *J. Ind. Eng. Chem.*, vol. 23, pp. 243–250, 2015.

[39] F. Chen, J. Ying, Y. Wang, S. Du, Z. Liu, and Q. Huang, "Effects of graphene content on the microstructure and properties of copper matrix composites," *Carbon N. Y.*, vol. 96, pp. 836–842, 2016.

[40] A. Saboori, K. S. Moheimani, M. Pavese, C. Badini, and P. Fino, "New Nanocomposite Materials with Improved Mechanical Strength and Tailored Coefficient of Thermal Expansion for Electro-Packaging Applications," *Metals* , vol. 7, no. 12. 2017.

[41] T. X. H. Le, M. Bechelany, S. Lacour, N. Oturan, M. A. Oturan, and M. Cretin, "High removal efficiency of dye pollutants by electron-Fenton process using a graphene based cathode," *Carbon N. Y.*, vol. 94, pp. 1003–1011, 2015.

[42] J. R. Carvajal, “Recent development of the Program FULLPROF,” *Comm. Powder Diffr. (IUCr), Newsl.*, vol. 26, pp. 12–19, 2001.

[43] M. F. Bekheet, L. Schlicker, A. Doran, K. Siemensmeyer, and A. Gurlo, “Ferrimagnetism in manganese-rich gallium and aluminium spinels due to mixed valence Mn2+–Mn3+ states,” *Dalt. Trans.*, vol. 47, no. 8, pp. 2727–2738, 2018.

[44] M. F. Bekheet, G. Miehe, C. Fasel, A. Gurlo, and R. Riedel, “Low temperature synthesis of nanocrystalline MnIn 2 O 4 spinel,” *Dalt. Trans.*, vol. 41, no. 12, pp. 3374–3376, 2012.

[45] R. Schmidt, S. Pandey, P. Fiorenza, and D. C. Sinclair, “Non-stoichiometry in ‘CaCu 3 Ti 4 O 12’(CCTO) ceramics,” *RSC Adv.*, vol. 3, no. 34, pp. 14580–14589, 2013.

[46] J. Li, M. A. Subramanian, H. D. Rosenfeld, C. Y. Jones, B. H. Toby, and A. W. Sleight, “Clues to the Giant Dielectric Constant of CaCu3Ti4O12 in the Defect Structure of ‘SrCu3Ti4O12,’” *Chem. Mater.*, vol. 16, no. 25, pp. 5223–5225, Dec. 2004.

[47] R. Schmidt *et al.*, “Effects of sintering temperature on the internal barrier layer capacitor (IBLC) structure in CaCu3Ti4O12 (CCTO) ceramics,” *J. Eur. Ceram. Soc.*, vol. 32, no. 12, pp. 3313–3323, 2012.

[48] T.-T. Fang and Y.-H. Wang, “Reassessment of copper and titanium valences and excess holes in oxygen 2p levels of CaCu3Ti4O12,” *J. Electrochem. Soc.*, vol. 158, no. 9, pp. G207–G210, 2011.

[49] M. C. Mozzati, C. B. Azzoni, D. Capsoni, M. Bini, and V. Massarotti, “Electron paramagnetic resonance investigation of polycrystalline CaCu3Ti4O12,” *J. Phys. Condens. Matter*, vol. 15, no. 43, p. 7365, 2003.

[50] M. A. Pires *et al.*, “Role of oxygen vacancies in the magnetic and dielectric properties of the high-dielectric-constant system ${\mathrm{CaCu}}_{3}{\mathrm{Ti}}_{4}{\mathrm{O}}_{12}$: An electron-spin resonance study,” *Phys. Rev. B*, vol. 73, no. 22, p. 224404, Jun. 2006.

[51] S. Orrego, J. A. Cortés, R. A. C. Amoresi, A. Z. Simões, and M. A. Ramírez, “Photoluminescence behavior on Sr2+ modified CaCu3Ti4O12 based ceramics,” *Ceram. Int.*, vol. 44, no. 9, pp. 10781–10789, Jun. 2018.

[52] H. Dai *et al.*, “Effect of BiFeO3 doping on the structural, dielectric and electrical properties of CaCu3Ti4O12 ceramics,” *Appl. Phys. A*, vol. 119, no. 1, pp. 233–240, 2015.

[53] C. Wang, H. J. Zhang, P. M. He, and G. H. Cao, “Ti-rich and Cu-poor grain-boundary layers of CaCu3Ti4O12 detected by x-ray photoelectron spectroscopy,” *Appl. Phys. Lett.*, vol. 91, no. 5, p. 52910, Jul. 2007.

[54] F. Wu, Y. Myung, and P. Banerjee, “Unravelling transient phases during thermal oxidation of copper for dense CuO nanowire growth,” *CrystEngComm*, vol. 16, no. 16, pp. 3264–3267, 2014.

[55] E. Manikandan, G. Kavitha, and J. Kennedy, “Epitaxial zinc oxide, graphene oxide composite thin-films by laser technique for micro-Raman and enhanced field emission

study," *Ceram. Int.*, vol. 40, no. 10, Part A, pp. 16065–16070, 2014.

[56] M. Sathish, B. Viswanathan, R. P. Viswanath, and C. S. Gopinath, "Synthesis, Characterization, Electronic Structure, and Photocatalytic Activity of Nitrogen-Doped TiO2 Nanocatalyst," *Chem. Mater.*, vol. 17, no. 25, pp. 6349–6353, Dec. 2005.

[57] X. Wang *et al.*, "Synthesis, structural characterization and evaluation of floating B-N codoped TiO2/expanded perlite composites with enhanced visible light photoactivity," *Appl. Surf. Sci.*, vol. 349, pp. 264–271, Sep. 2015.

[58] B. Bharti, S. Kumar, H.-N. Lee, and R. Kumar, "Formation of oxygen vacancies and Ti3+ state in TiO2 thin film and enhanced optical properties by air plasma treatment," *Sci. Rep.*, vol. 6, p. 32355, Aug. 2016.

[59] M. Liu, X. Qiu, M. Miyauchi, and K. Hashimoto, "Cu(II) Oxide Amorphous Nanoclusters Grafted Ti3+ Self-Doped TiO2: An Efficient Visible Light Photocatalyst," *Chem. Mater.*, vol. 23, no. 23, pp. 5282–5286, Dec. 2011.

[60] G. Blasse and B. C. Grabmaier, "How Does a Luminescent Material Absorb Its Excitation Energy? BT - Luminescent Materials," G. Blasse and B. C. Grabmaier, Eds. Berlin, Heidelberg: Springer Berlin Heidelberg, 1994, pp. 10–32.

[61] P. Y. Raval *et al.*, "First observation of reversible mechanochromism and chromaticity study on calcium–copper–titanate," *J. Am. Ceram. Soc.*, vol. 102, no. 11, pp. 6872–6881, Nov. 2019.

[62] L. H. Oliveira *et al.*, "Correlation Between Photoluminescence and Structural Defects in Ca1+xCu3−xTi4O12 Systems," *J. Am. Ceram. Soc.*, vol. 96, no. 1, pp. 209–217, Jan. 2013.

[63] A. A. Felix, M. Spreitzer, D. Vengust, D. Suvorov, and M. O. Orlandi, "Probing the effects of oxygen-related defects on the optical and luminescence properties in CaCu3Ti4O12 ceramics," *J. Eur. Ceram. Soc.*, vol. 38, no. 15, pp. 5002–5006, 2018.

[64] M. Wang and L. Zhang, "The influence of orientation on the photoluminescence behavior of ZnO thin films obtained by chemical solution deposition," *Mater. Lett.*, vol. 63, no. 2, pp. 301–303, 2009.

[65] J. Wang and W.-D. Zhang, "Modification of TiO2 nanorod arrays by graphite-like C3N4 with high visible light photoelectrochemical activity," *Electrochim. Acta*, vol. 71, pp. 10–16, 2012.

[66] C. Wu *et al.*, "Ti3+ self-doped TiO2 photoelectrodes for photoelectrochemical water splitting and photoelectrocatalytic pollutant degradation," *J. Energy Chem.*, vol. 25, no. 4, pp. 726–733, 2016.

[67] S. Wang *et al.*, "Defective black Ti3+ self-doped TiO2 and reduced graphene oxide composite nanoparticles for boosting visible-light driven photocatalytic and photoelectrochemical activity," *Appl. Surf. Sci.*, vol. 467–468, pp. 45–55, 2019.

[68] Z. Zhang, X. Yang, M. N. Hedhili, E. Ahmed, L. Shi, and P. Wang, "Microwave-Assisted Self-Doping of TiO2 Photonic Crystals for Efficient Photoelectrochemical Water Splitting," *ACS Appl. Mater. Interfaces*, vol. 6, no. 1, pp. 691–696, Jan. 2014.

[69] K. Lee *et al.*, “Cu+-incorporated TiO2 overlayer on Cu2O nanowire photocathodes for enhanced photoelectrochemical conversion of CO2 to methanol,” *J. Energy Chem.*, vol. 27, no. 1, pp. 264–270, 2018.

[70] S. Kawrani *et al.*, “Enhancement of calcium copper titanium oxide photoelectrochemical performance using boron nitride nanosheets,” *Chem. Eng. J.*, vol. 389, p. 124326, 2020.

[71] H. Liu, X. Z. Li, Y. J. Leng, and W. Z. Li, “An Alternative Approach to Ascertain the Rate-Determining Steps of TiO2 Photoelectrocatalytic Reaction by Electrochemical Impedance Spectroscopy,” *J. Phys. Chem. B*, vol. 107, no. 34, pp. 8988–8996, Aug. 2003.

[72] W. H. Leng, Z. Zhang, J. Q. Zhang, and C. N. Cao, “Investigation of the Kinetics of a TiO2 Photoelectrocatalytic Reaction Involving Charge Transfer and Recombination through Surface States by Electrochemical Impedance Spectroscopy,” *J. Phys. Chem. B*, vol. 109, no. 31, pp. 15008–15023, Aug. 2005.

[73] G. Applerot *et al.*, “Understanding the Antibacterial Mechanism of CuO Nanoparticles: Revealing the Route of Induced Oxidative Stress,” *Small*, vol. 8, no. 21, pp. 3326–3337, Nov. 2012.

[74] B. Fahmy and S. A. Cormier, “Copper oxide nanoparticles induce oxidative stress and cytotoxicity in airway epithelial cells,” *Toxicol. Vitr.*, vol. 23, no. 7, pp. 1365–1371, Oct. 2009.